



Synthesis and Characterization of Iron-Doped TiO₂ Nanoparticles Using Ferrocene from Flame Spray Pyrolysis

Item Type	Article
Authors	Ismail, Mohamed;Hedhili, Mohamed N.;Anjum, Dalaver H.;Singaravelu, Venkatesh;Chung, Suk Ho
Citation	Ismail, M. A., Hedhili, M. N., Anjum, D. H., Singaravelu, V., & Chung, S. H. (2021). Synthesis and Characterization of Iron-Doped TiO ₂ Nanoparticles Using Ferrocene from Flame Spray Pyrolysis. <i>Catalysts</i> , 11(4), 438. doi:10.3390/catal11040438
Eprint version	Publisher's Version/PDF
DOI	10.3390/catal11040438
Publisher	MDPI AG
Journal	Catalysts
Rights	This article is an open access article distributed under the terms and conditions of the Creative Commons Attribution (CC BY) license.
Download date	2024-04-17 07:28:40
Item License	https://creativecommons.org/licenses/by/4.0/
Link to Item	http://hdl.handle.net/10754/668492

Article

Synthesis and Characterization of Iron-Doped TiO₂ Nanoparticles Using Ferrocene from Flame Spray Pyrolysis

Mohamed Anwar Ismail ^{1,*} , Mohamed N. Hedhili ² , Dalaver H. Anjum ^{2,3}, Venkatesh Singaravelu ⁴ and Suk Ho Chung ⁵

¹ Mechanical Power Engineering Department, Faculty of Engineering, Zagazig University, Zagazig 44519, Egypt

² Imaging and Characterization Core Lab, King Abdullah University of Science and Technology (KAUST), Thuwal 23955-6900, Saudi Arabia; mohamed.hedhili@kaust.edu.sa (M.N.H.); dalaver.anjum@ku.ac.ae (D.H.A.)

³ Department of Physics, Khalifa University, Abu Dhabi 127788, United Arab Emirates

⁴ Physical Sciences and Engineering Division, King Abdullah University of Science and Technology (KAUST), Thuwal 23955-6900, Saudi Arabia; venkatesh.singaravelu@kaust.edu.sa

⁵ Clean Combustion Research Center (CCRC), King Abdullah University of Science and Technology (KAUST), Thuwal 23955-6900, Saudi Arabia; sukho.chung5@gmail.com

* Correspondence: manwar@zu.edu.eg; Tel.: +20-109-526-1960

Abstract: Iron-doped titanium dioxide nanoparticles, with Fe/Ti atomic ratios from 0% to 10%, were synthesized by flame spray pyrolysis (FSP), employing a single-step method. Ferrocene, being nontoxic and readily soluble in liquid hydrocarbons, was used as the iron source, while titanium tetraisopropoxide (TTIP) was used as the precursor for TiO₂. The general particle characterization and phase description were examined using ICP-OES, XRD, BET, and Raman spectroscopy, whereas the XPS technique was used to study the surface chemistry of the synthesized particles. For particle morphology, HRTEM with EELS and EDS analyses were used. Optical and magnetic properties were examined using UV–vis and SQUID, respectively. Iron doping to TiO₂ nanoparticles promoted rutile phase formation, which was minor in the pure TiO₂ particles. Iron-doped nanoparticles exhibited a uniform iron distribution within the particles. XPS and UV–vis results revealed that Fe²⁺ was dominant for lower iron content and Fe³⁺ was common for higher iron content and the iron-containing particles had a contracted band gap of ~1 eV lower than pure TiO₂ particles with higher visible light absorption. SQUID results showed that doping TiO₂ with Fe changed the material to be paramagnetic. The generated nanoparticles showed a catalytic effect for dye-degradation under visible light.

Keywords: flame synthesis; flame spray pyrolysis; titanium dioxide; iron-doping; dye degradation



Citation: Ismail, M.A.; Hedhili, M.N.; Anjum, D.H.; Singaravelu, V.; Chung, S.H. Synthesis and Characterization of Iron-Doped TiO₂ Nanoparticles Using Ferrocene from Flame Spray Pyrolysis. *Catalysts* **2021**, *11*, 438. <https://doi.org/10.3390/catal11040438>

Academic Editor:
Anna Zielińska-Jurek

Received: 26 February 2021
Accepted: 25 March 2021
Published: 29 March 2021

Publisher's Note: MDPI stays neutral with regard to jurisdictional claims in published maps and institutional affiliations.



Copyright: © 2021 by the authors. Licensee MDPI, Basel, Switzerland. This article is an open access article distributed under the terms and conditions of the Creative Commons Attribution (CC BY) license (<https://creativecommons.org/licenses/by/4.0/>).

1. Introduction

Flame spray pyrolysis (FSP) has emerged as a cost-effective method for large-scale synthesis of nanoparticles [1] and a number of large-scale pilot projects based on FSP have been recently demonstrated [2]. The Johnson-Matthey Company announced the use of FSP for the exploration of next-generation materials related to catalytic applications [3]. Wegner et al. [2], demonstrated that FSP can be used to produce nanoparticles at a rate of a few kilograms per hour at a cost below 100 EUR/kg, where chemical precursors account for the majority of the cost. It is critical to explore research in different precursors for use in FSP, where future innovation may occur at the juncture of combustion, material, and aerosol engineering.

Titanium dioxide (TiO₂) is widely produced using flame-based methods [4–6] for various applications in catalysis, water-treatment, and solar cells. Doping TiO₂ nanoparticles with transition metals, such as Fe and Co, can result in better photocatalytic conversions due to a reduction in the band-gap and the recombination rate of the electron hole pair [7–9].

Additionally, such transition metals can be used to produce TiO₂ nanoparticles with dilute magnetic semiconductor properties [10] that are important for spintronics applications.

Wet-chemistry methods have been utilized to synthesize iron-doped titania nanoparticles [11–14]. To obtain crystallized nanoparticles from such methods, many steps are involved during the synthesis process in addition to post annealing, which may result in phase segregation at higher iron content (Fe 3 at.% and more) [13]. Single-step production of Fe-TiO₂ nanoparticles is the main advantage in adopting gas-phase techniques of nanoparticle synthesis. Wang et al. [13] produced iron-doped titania with iron content from 0% to 20% using an radiofrequency (RF) plasma. Their major finding was that iron-doping advanced the change from anatase to rutile nanoparticles. Teoh et al. [15] utilized a flame spray pyrolysis method in generating iron-doped titania. They used titanium tetraisopropoxide as the titanium precursor and iron naphthenate as the iron precursor. FSP increased the iron-doping up to five times higher than conventional methods with annealing. Increasing Fe concentration results in the transformation from anatase to rutile phase nanoparticles. Fe-TiO₂ nanoparticles were active under visible light and the rate of oxalic acid mineralization is 6.4 times greater when compared to pure TiO₂ and Degussa P25. Magnetic properties were not reported for the FSP-made Fe-TiO₂ nanoparticles.

Ferrocene has many properties, which make it a suitable source of iron for iron-doping in titania nanoparticles such as nontoxicity, stability, and solubility in liquid hydrocarbons [16]. Ferrocene, as a fuel additive for soot reduction, has been broadly considered in the combustion community [16,17]. Ferrocene, as a catalyst, has been utilized in synthesis of carbon nanotubes [18,19] and silica nanoparticles with a controlled surface area in diffusion flames [20]. Ferrocene was used in FSP as a co-precursor for the production of carbon nano-tubes (CNTs) [21,22], boron nitride/carbon nano-tube composite (BN/CNTs) [23], and metal oxides as Al₂O₃ [24], Fe₂O₃ [25], and thin films [26]. However, as far as the authors' aware, ferrocene has not been used as an iron source in generating iron-doped titania from FSP technique.

In this work, ferrocene was utilized as an iron precursor and titanium tetraisopropoxide (TTIP) was utilized as a titanium precursor to synthesize iron-doped TiO₂ nanoparticles. Various characterization techniques were performed to study the phase, morphology, and surface structure of the nanoparticles. Optical and magnetic properties were measured. Finally, the doped-particles were used as a photocatalyst for dye-degradation experiments under visible light.

2. Results and Discussion

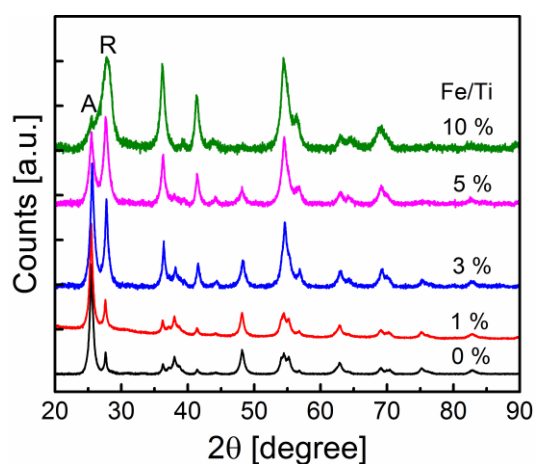
2.1. General Nanoparticle Characterization

To estimate the accurate amount of iron doped in TiO₂ samples, inductively-coupled plasma-optical emission spectrometry (ICP-OES) was implemented (Table 1). Direct proportionality was noticed between amounts of ferrocene added to the iron content found in each Fe-TiO₂ sample. The percentage of iron in the doped samples ranged from 0.87% to 5.24 at.%. The specific surface area results utilizing Brunauer–Emmett–Teller (BET) nitrogen adsorption experiments are shown in Table 1. A specific surface area (SSA) for the iron-free TiO₂ sample was the highest and had a value of 151 m²/g, while it was dropped to 118 m²/g when the Fe/Ti atomic ratio was 1%. Then it was raised monotonically with iron content in the doped-sample. The average primary particle diameter d_{BET} was calculated from BET results while assuming spherical nanoparticles [27]. It was found that d_{BET} was around 10 nm for most samples.

Table 1. Fe-doped TiO₂ synthesis conditions and properties.

Precursor (control)	Synthesized (ICP)	SSA (BET)	d_{BET}	Anatase	d_{XRD}
Fe/Ti %	Fe in Fe-TiO ₂ %				
0	0.0	151	9.9	91.8	16.2
1	0.87	118	12.6	85.8	18.8
3	1.56	137	10.9	64.2	16.3
5	2.61	139	10.4	42.1	12.2
10	5.24	140	10.2	20.9	15.9

Nanoparticle structure and crystallinity was identified using the X-ray diffraction (XRD) technique. Figure 1 illustrates the XRD pattern for Fe-doped samples compared to pure TiO₂ nanoparticles, revealing peaks at $2\theta \cong 25.4$ (for anatase 101) and 27.5 (for rutile 110) crystalline phases. The dominant phase found in the pure TiO₂ nanoparticles was anatase, which is typical for TiO₂ flame synthesis under lean conditions [28], while Fe-doping tended to promote the rutile phase percentage and reduces the anatase percentage with increasing iron content in the sample [29]. At 10% of iron-doping, the rutile phase was dominant. By integrating the respective XRD peak intensities, anatase content could be calculated [30]. A calculated anatase percentage for various samples are listed in Table 1. Fe can occupy the Ti position in the TiO₂ lattice because Fe³⁺ and Ti⁴⁺ have similar ionic radii [31]. These results are in agreement with previously published data for Fe-TiO₂ using gas-phase methods [13,15].

**Figure 1.** XRD spectra for iron-doped samples compared to pure TiO₂ nanoparticles.

Scherrer formula [32] is another method that gives a good indication of the crystallite size d_{XRD} by estimating the position of main anatase (101) and rutile (110) peaks. It was observed that d_{XRD} for all analyzed samples ranges from 12 to 19 nm, as shown in Table 1. To emphasize the various phases existing in the synthesized TiO₂ nanoparticles, Raman spectroscopy was carried out, as shown in Figure 2. Anatase was the dominant phase for iron-free TiO₂ particles, whereas the rutile phase was the dominant phase for iron-doped particles. The Raman data were consistent with the XRD results.

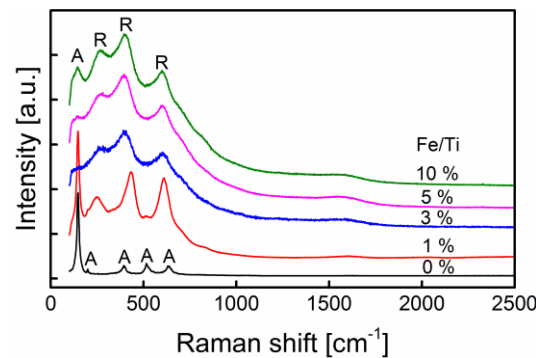


Figure 2. Raman spectra for Fe-doped TiO₂ nanoparticles prepared by FSP with various Fe ratios (A, anatase. R, rutile).

2.2. Fe-TiO₂ Morphology

Bright-field TEM (BF-TEM) along with energy-dispersive X-ray spectroscopy (EDS) analyses were carried out to examine the overall elemental composition and quality of the iron-doped TiO₂ particles. Several electron micrographs at low magnification and EDS spectra were acquired from various locations on the grid for a good representation of size and composition. Figure 3a–c show typical electron micrographs for pure TiO₂ and Fe-TiO₂ nanoparticles. Iron-free particles have an average size of 12 nm. The particle morphology in iron-doped cases (Fe/Ti ratio of 3% and 10%) is similar to that of the iron-free TiO₂ case. The selected area electron diffraction (SAED) micrographs (Figure 3a–c insets) contain diffraction rings that confirm the synthesized nanoparticles were of anatase and rutile phases (also confirmed by XRD and Raman results). Figure 3d–f illustrates the high resolution TEM (HRTEM) electron micrographs for pure and iron-doped TiO₂ nanoparticles. All analyzed samples showed high crystallinity as well as an ordered lattice structure.

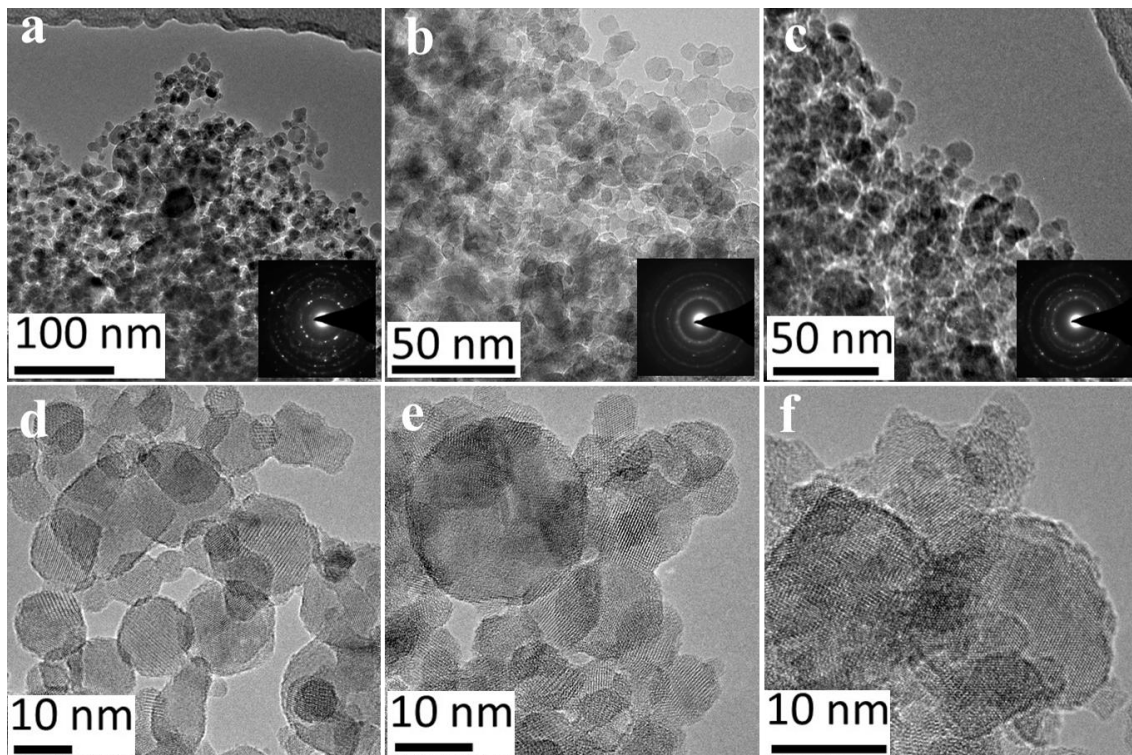


Figure 3. TEM (a–c) with SAED pattern (inset) and HRTEM (d–f) for samples with an Fe/Ti ratio of: (a,d) 0%, (b,e) 3%, and (c,f) 10%.

Figure 4a–c show higher magnification of HRTEM images and illustrates the interplanar spacing (d-spacing) of the planes for TiO_2 phases of selected samples. It indicates the decrease in d-spacing with an increase of the iron content in the sample. For pure TiO_2 nanoparticles, the d-spacing of 0.354 nm is related to (101) anatase planes, whereas the value of 0.327 nm for iron doped sample with Fe/Ti ratio of 10% is related to (110) rutile planes [33]. This phase change from anatase to rutile when increasing the iron content is in good agreement with the previous results. The statistical analysis of particle size distribution obtained from TEM results was based on more than 150 nanoparticles and the size distribution histograms are provided in Figure 4d–f. It could be concluded that more than 95% of the particles have a diameter between 7 and 19 nm. The particle size distribution does not change much with doping iron in the TiO_2 samples.

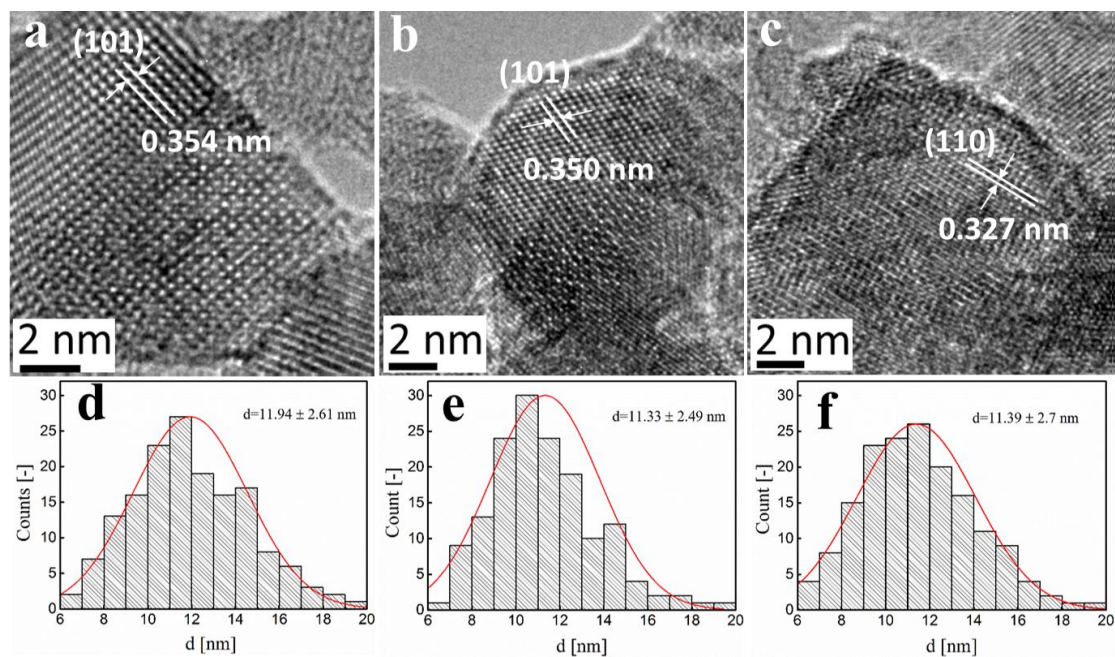


Figure 4. HRTEM images and particle size distribution for samples with an Fe/Ti ratio of: (a,d) 0%, (b,e) 3%, and (c,f) 10%.

Figure 5 shows the data revealed from EDS spectra, which confirms the existence of both Ti and O elements in the iron-free TiO_2 sample. For the 3% (Fe/Ti atomic ratio) sample, the Fe peak started to appear and its intensity increased for higher iron-doping (Fe/Ti = 10%) with an additional Fe peak, which indicates a higher iron concentration in the nanoparticles. In addition, a small Cu peak is observed in the sample with higher iron concentration. Additional Cu peaks observed in the spectrum are attributed to the Cu-grid.

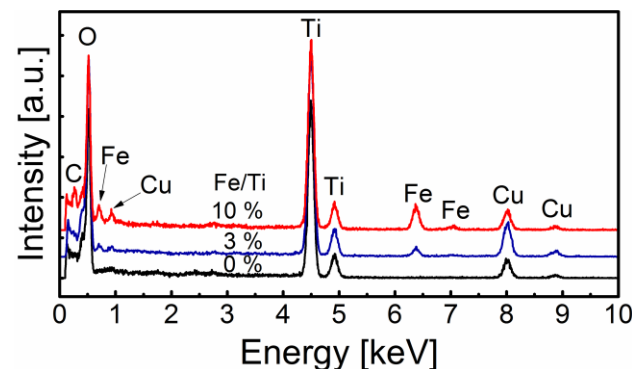


Figure 5. EDS spectra acquired from the region of Figure 4, revealing the existence of Fe in Fe- TiO_2 nanoparticles.

The presented electron energy-loss spectroscopy (EELS) spectra in Figure 6 contain the energy loss edges of Ti, O, and Fe elements. The energy loss edge of Ti at the energy loss value of 456 eV is Ti-L23 and it represents electron beam-induced electronic transitions in Ti atoms from the initial states of $2P_{1/2}$ and $2P_{3/2}$ to final states of $3S$ or $3P$ orbitals. Similarly, the energy of edge of Fe at the energy loss value of 710 eV is Fe-L23 and it also represents the same electronic transitions in Fe atoms as of Ti atoms. Whereas the energy loss edge of O at the energy value of 532 eV is the O-K edge, it represents the electronic transitions from $1S_{1/2}$ initial states to $2P$ final states in O atoms. The intensity of signals of these energy loss edges is proportional to the elemental composition of nanomaterials and, therefore, have been utilized to map the spatial distributions of these elements in the samples. More detailed analysis for EDS and EELS results can be found in Reference [34]. The acquired elemental maps of the 10% sample are presented in Figure 7. The results demonstrated that Ti, O, and Fe were present and reasonably uniform, implying that Fe was uniformly doped in the TiO_2 nanoparticles and did not contain segregated iron oxide particles.

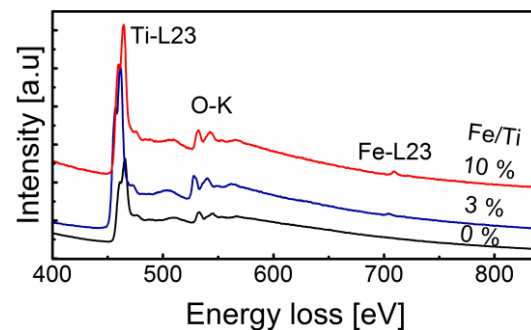


Figure 6. Core-loss EELS analysis of TiO_2 and Fe- TiO_2 samples. Spectra contain edges of all elements present in these samples.

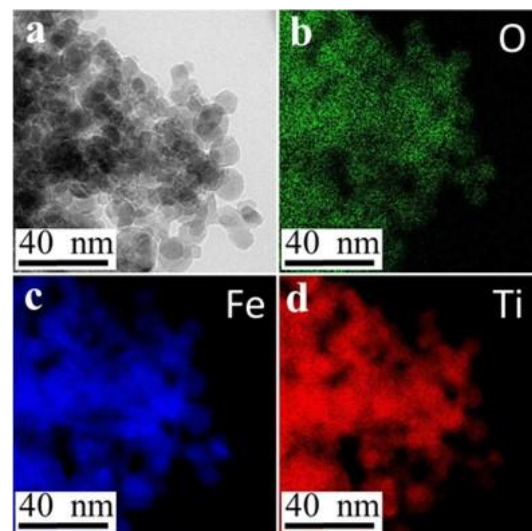


Figure 7. Elemental mapping of 10% Fe in TiO_2 nanoparticles indicating (a) raw TEM image, (b, c, and d) are (O, Fe, and Ti) elemental maps, respectively.

2.3. Surface Chemistry

Chemical composition was analyzed using X-ray photoelectron spectroscopy (XPS). Survey spectra from pure TiO_2 and from Fe-doped TiO_2 samples are shown in Figure 8. Ti, O, C, and Fe elements are detected for the iron-doped samples whereas Fe was not detected from pure TiO_2 sample. It should be noted that the synthesized samples do not contain any carbon while the carbon peak in the survey scan comes from the background. High resolution XPS spectra of Ti 2p and O 1s core levels from pure TiO_2 are shown in

Figure 9. The Ti $2p_{3/2}$ core level is fitted using two components. The dominant peak centered at 458.6 eV is associated with Ti ions with a formal valence 4+ (Ti^{4+}), while the peak at the lower binding energy of ~ 456.6 eV is associated with Ti ions with a reduced charge state (Ti^{3+}) [35]. The O 1s core level is centered at 529.8 eV, corresponding to the metal oxide (TiO_2) [35]. These Ti 2p and O 1s peaks are also observed for all the Fe-doped TiO_2 samples.

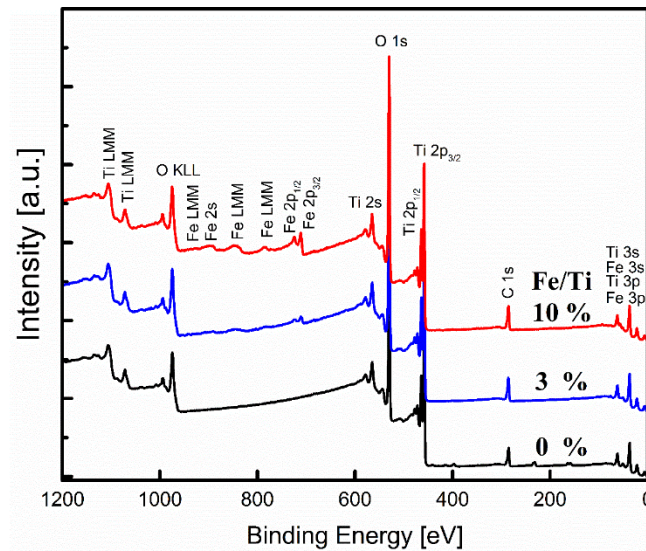


Figure 8. Survey scan spectra of pure TiO_2 and Fe-doped nanoparticles.

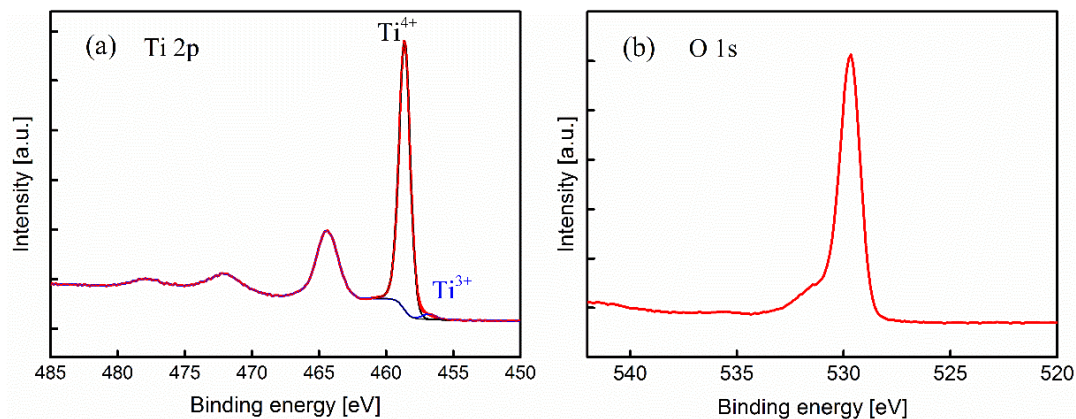


Figure 9. High resolution spectra of TiO_2 nanoparticles showing (a) Ti 2p peak and (b) O 1s peak for pure TiO_2 .

Figure 10 illustrates high resolution XPS spectra for iron-doped TiO_2 nanoparticles resulting from the Fe 2p core level. High resolution data was fitted using eight components located at 710.8, 709.1, 718.3, 719.4, 722.3, 724.2, 728.5, and 732.9 eV. The Fe $2p_{3/2}$ doublet peak at 710.8 eV, and its corresponding satellite peak at 719.4 eV, together with the Fe $2p_{1/2}$ doublet peak at 724.3 eV, and its corresponding satellite peak at 732.9 eV, are the main signature of the Fe^{3+} oxidation state of Fe [36,37]. Another signature of Fe^{3+} ions are the satellite peaks located at 8.6 eV from the main peaks.

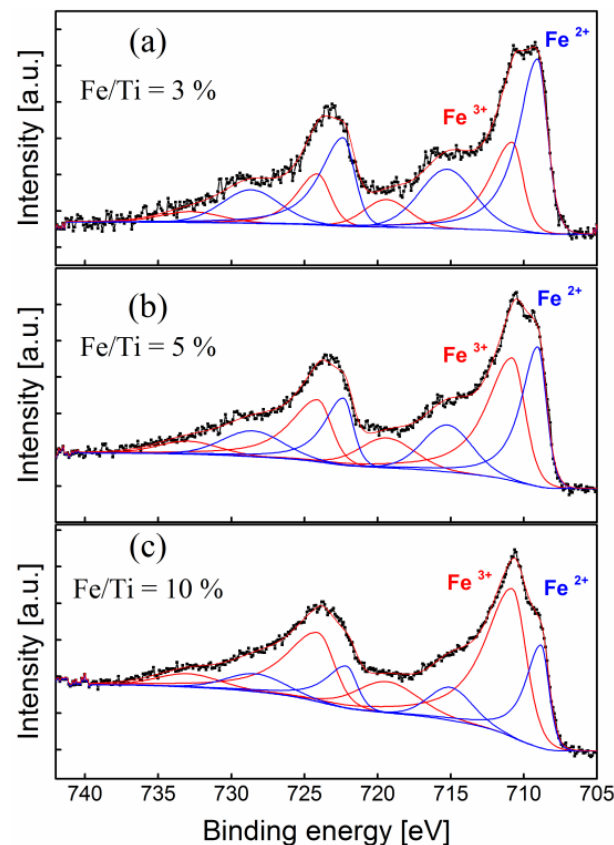


Figure 10. High resolution spectra for iron-doped samples resulting from Fe 2p peaks with an Fe/Ti ratio of (a) 3%, (b) 5%, and (c) 10%.

The Fe $2p_{3/2}$ doublet peak at 709.1 eV and its corresponding satellite peak at 715.3 eV, together with the Fe $2p_{1/2}$ doublet peak at 722.3 eV and its corresponding satellite peak at 728.5 eV are signatures of the Fe^{2+} oxidation state of Fe [37,38]. Other signatures of Fe^{2+} ions are the satellite peaks located at 6.2 eV from the main peaks. The area ratio of Fe $2p_{3/2}$ –Fe $2p_{1/2}$ components equals 2:1 with their doublet separation of 13.5 and 13.2 eV for Fe^{3+} and Fe^{2+} , respectively. The same values are used for their corresponding satellites. Increasing the percentage of the Fe dopant leads to an increase of the Fe^{3+}/Fe^{2+} ratio from 0.5 at 3% (Fe/Ti ratio) to 1.8 at 10% (Fe/Ti ratio).

The valence band spectra from pure and Fe-doped TiO_2 nanoparticles are shown in Figure 11. The spectrum of undoped TiO_2 contained three major features (marked as A, B, and C) at binding energy positions around ~ 7.5 , 5, and 1 eV, respectively. This is consistent with the literature [39]. Features A and B are related to the O-2p derived states and are referred to as ‘bonding’ and ‘non-bonding orbital emissions,’ respectively. Feature C corresponds to the Ti^{3+} 3d defect state. After Fe doping, feature D (~ 2.5 eV) began to appear. Such a shape, based on the literature, is assigned to a mixed Fe 3d and Ti 3d derived states [39]. Note that the valence band edge from the Fe-doped TiO_2 shifted by ~ 1 eV to a lower binding energy, compared to undoped TiO_2 , which could enhance photo-catalytic properties in the region of visible light [40].

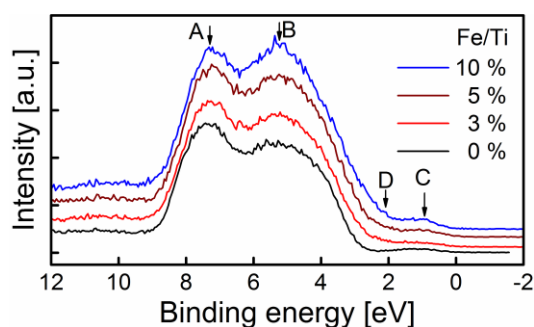


Figure 11. Valance band for TiO_2 and Fe-doped TiO_2 samples, indicating structures A, B, and C for TiO_2 and structure D for Fe.

2.4. Magnetic Properties

To study the intrinsic magnetic property, temperature variations of magnetization measurements (moment M vs. temperature T) were performed. Initially, the sample was cooled to 5 K under a nominal zero field. Then a field of $H = 1$ kOe was applied. Subsequently, M vs. T data was measured under the constant magnetic field, while warming the sample from 5 K to 300 K (Figure 12). Results showed that all the samples were typical paramagnetic and none showed any Curie transition (TC), within the temperature range, which implies that Fe doping did not induce a long range of a ferromagnetic interaction in these samples.

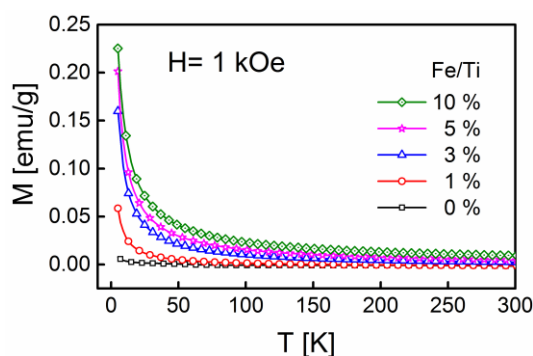


Figure 12. Temperature-dependent magnetizations measured under a constant magnetic field of 1 kOe.

Isothermal magnetization measurements (magnetic moment M vs. magnetic field H) were carried out. A necessary diamagnetic correction corresponding to the bare sample holder was applied after magnetization measurements on each sample. Figure 13 shows the magnetic hysteresis (M - H) curves of the undoped and Fe-doped samples taken at 5 and 300 K. The results showed that magnetization increases monotonically with increased Fe content. At room temperature, most of the doped samples have small moment values, which is similar to the undoped sample. However, for the 10% case, a higher moment was observed. The inset in Figure 13b shows a narrow opening of the hysteresis loop near the origin for the 10% case, indicating a paramagnetic behavior. Earlier reports attributed the absence of ferromagnetism (or paramagnetism in Fe- TiO_2) to sample preparation methods and/or dopant concentrations [41] where dopant Fe ions remain as isolated ions weakly interacting in the host TiO_2 . The lack of magnetic properties in previous works was also attributed to the presence of secondary phases, such as $\alpha\text{-Fe}_2\text{O}_3$ or Fe_3O_4 , since iron ions may coexist in different valance states [42,43]. For magnetic behavior, oxygen defects [41,44,45] could induce magnetic interactions. Since only paramagnetic properties were observed in the present study, it was attributed to oxygen defects and Fe^{3+} ions in the TiO_2 crystal.

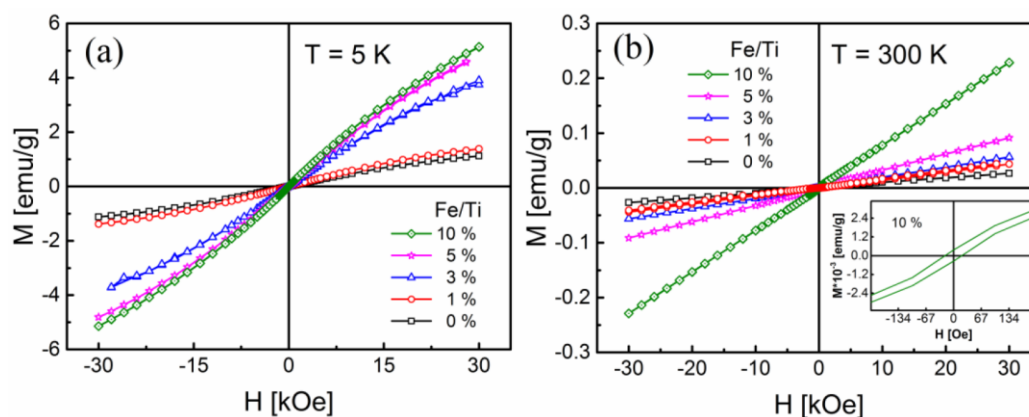


Figure 13. Magnetization (M - H) curves for iron-doped TiO_2 nanoparticles compared to pure TiO_2 measured under an external magnetic field (H), from -30 to 30 kOe at temperatures of (a) 5 K and (b) 300 K.

2.5. Optical Properties

The UV-vis absorption spectroscopy was adopted to determine light absorption from iron-free and iron-doped TiO_2 nanoparticles. The spectra are shown in Figure 14. The pure TiO_2 sample did not show any absorption in the region of visible light (>400 nm) whereas it manifested an absorption edge toward the UV region (<400 nm). This absorption peak could be assigned to anatase band-gap excitation, which equals 3.2 eV [31]. The visible light absorption (350 – 550 nm) was significantly increased by iron doping in TiO_2 nanoparticles and monotonically increased with iron content in the sample. This observation is consistent with data found in literature [46,47]. The powder color converted from white (pure TiO_2) by passing through yellow (low iron content) to brown (high iron content), indicating that doping TiO_2 nanoparticles with iron enhanced the visible light absorption.

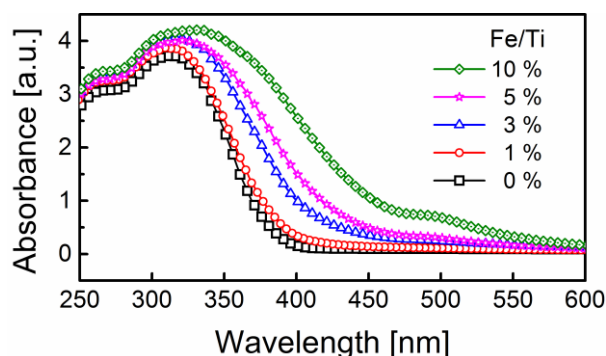


Figure 14. Ultraviolet-visible (UV-vis) spectra for iron-free and iron-doped TiO_2 nanoparticles.

3. Photocatalytic Application

3.1. Photocatalytic Activity Test

A photocatalytic reactor system was utilized to carry out the photodegradation tests of Rhodamine B (Rh-B) solution with iron-doped TiO_2 nanoparticles under visible-light irradiation. A mass equals 40 mg of iron-doped TiO_2 nanoparticles (as a catalyst) was added to 100 mL of organic dye solution (20 mg/L). Then the mixture was stirred in dark for 60 min to reach an adsorption-desorption equilibrium before performing the photodegradation experiments. The reactor was loaded up with the mixture of catalyst and organic dye solution. Water cooling was used to maintain the temperature constant at 298 K. Then, a Xenon lamp (CX-04E) with an optical filter (>420 nm) passing only visible light was used to irradiate the suspension. At a time interval of 15 min, about 2 mL of the suspension was extracted and centrifuged at $14,000$ rpm for a period of 5 min in order to get rid of the catalyst. To calculate the new dye concentration in the solution, absorbance at

$\lambda_{\max} = 553$ nm (maximum absorption peak of Rh-B) was measured and given the symbol C. The rate of dye degradation is recorded as C/C_0 where C_0 is the initial concentration after reaching the adsorption-desorption equilibrium.

3.2. Degradation of Rhodamine B

It was clear from the previous characterization of Fe-TiO₂ nanoparticles that iron doping shifted the optical response of TiO₂ nanoparticles from UV to the visible light region. The optical response was directly proportional to iron concentration in the iron-doped samples. This implied that these iron-doped TiO₂ nanoparticles, unlike iron-free TiO₂, could be active in the visible-light region and considered to be catalysts.

Since Rhodamine B is considered a major source of pollution for industrial waste water, its degradation in an aqueous solution has been studied. Figure 15 illustrates that, in the presence of iron-doped nanoparticles with Fe/Ti = 10%, the absorbance (at $\lambda_{\max} = 553$ nm) of the Rh-B dye monotonically decreases with time. The degradation efficiency of Rh-B dye in the presence of iron-doped TiO₂ catalysts have been calculated from the following equation.

$$D\% = \left[1 - \frac{C}{C_0} \right] \times 100 \quad (1)$$

where C_0 is the initial concentration of dye and C is the concentration of dye after irradiation in a selected time interval.

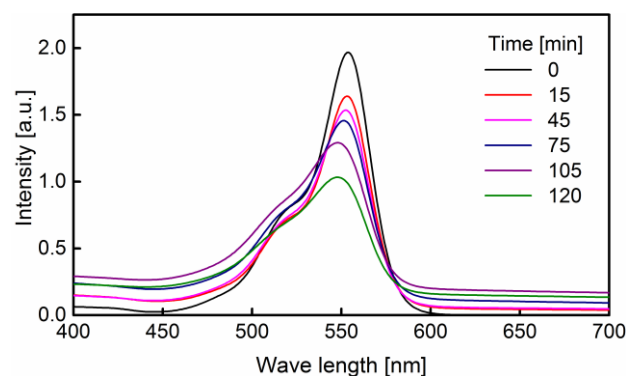


Figure 15. Absorption spectra of Rh-B dye in the existence of the Fe/Ti = 10% sample at various irradiation times.

The Rh-B dye concentration in the solution and its absorbance at $\lambda_{\max} = 553$ nm are directly proportional according to Beer's law. C_0 was considered to be the initial concentration of Rh-B dye in the solution to make sure that only a chemical reaction changes the dye concentration and removes any effect of dark adsorption.

Figure 16 illustrates the Rh-B dye degradation rates in the existence of iron-free TiO₂ and iron-doped TiO₂ nanoparticles under visible-light radiation. When using pure TiO₂ nanoparticles as a catalyst for two hours of radiation, the dye was degraded by ~12% and the degradation efficiency was raised to 20% when using an iron-doped sample with Fe/Ti = 1%. Then it was monotonically increased up to 53% when using an iron-doped sample with Fe/Ti = 10%. The degradation efficiencies of Rh-B dye in an aqueous solution in the current study are consistent with values in literature [14,48,49]. After absorbing light, the excited dye (Rhodamine B) injected an electron into the conduction band of TiO₂ where it was captured by surface-adsorbed O₂ to form O₂^{•−}. Then, the dye cation radicals were degraded via attack by oxygen active species [50]. In addition, it was noticed that no Rh-B dye degradation took place under visible-light radiation without catalysts.

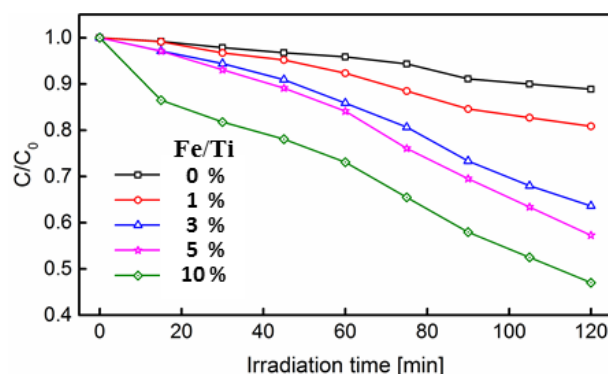


Figure 16. Rhodamine B concentration vs. irradiation time in the existence of Fe-TiO₂ nanoparticles.

The first-order rate constant k (min⁻¹) for photodegradation of dyes has been calculated by employing the following equation:

$$\ln C = \ln C_0 - kt \quad (2)$$

where C_0 and C are dye concentrations initially and after time t , respectively. The photodegradation rate constant (k) could be calculated from the above kinetic model and found to have the value of 0.001, 0.0019, 0.0039, 0.0047, and 0.006 min⁻¹ for samples Fe/Ti = 0%, 1%, 3%, 5%, and 10%, respectively. Previous studies showed that the rate constant of Rh-B photodegradation had reported a value of 0.0029 min⁻¹ when using iron-doped titania and 0.00016 min⁻¹ when using P25 [48]. Higher rate constants for the decomposition of Rh-B of the synthesized materials than standard P25 and Fe-TiO₂ NPs prepared using different methods suggested that the present materials are more active. Hence, the above findings clearly demonstrate that a higher amount of iron incorporation into the framework of TiO₂ makes the catalyst more efficient for photocatalytic degradation of organic dyes.

4. Experiment

FSP was applied to synthesize TiO₂ and Fe-TiO₂ nanoparticles. Figure 17 shows the schematic of experimental setup, composed of a spray system with an annular pilot flame, a precursor delivery system, and a particle collection system. The spray system was an air-assisted spray nozzle. The precursor flowed through a capillary tube while the dispersion gas passed through the annular gap. Dispersion gas of oxygen (10.6 L/min) was supplied to the spray nozzle for precursor atomization with a pressure drop across the nozzle of 2.5 bar. An annular slit (15.88 mm inner diameter and 1 mm thickness), surrounding the nozzle provided the supporting premixed pilot flame. Methane (CH₄ with purity 99.995%) with a flow rate of 1.25 L/min was mixed with 2.5 L/min of oxygen (O₂ with purity 99.9995%) for the pilot flame.

Various precursors were used to synthesize pure and doped-TiO₂ nanoparticles. Titanium tetraisopropoxide (Sigma-Aldrich, 97% purity) for TiO₂ nanoparticles (NP), and dissolving ferrocene (Sigma-Aldrich, 98%) in *m*-xylene (Sigma-Aldrich, 99%) for Fe doping. Table 1 shows the Fe/Ti atomic ratios in synthesizing nanoparticles resulting from changing ferrocene concentration. A syringe pump was used to inject the precursor into the spray nozzle with a flow rate of 450 mL/hr. Synthesized nanoparticles were collected on a glass-fiber filter with the aid of a vacuum pump.

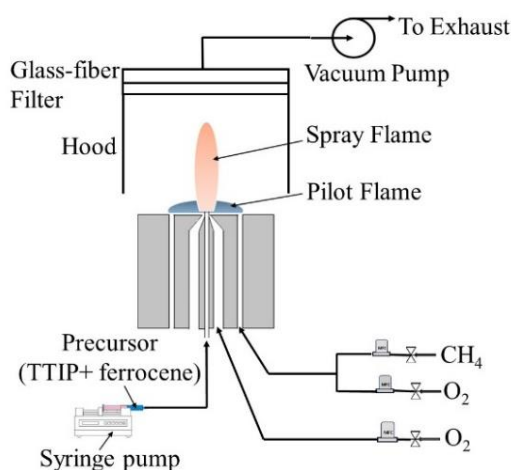


Figure 17. Schematic of flame spray pyrolysis (FSP) apparatus.

Phase and iron-content in the synthesized nanoparticles were identified by X-ray diffraction (Bruker, D8) using radiation from $\text{CuK}\alpha$ ($\lambda = 1.5406 \text{ \AA}$), Raman spectroscopy (Aramis, LabRAM HR Visible) with 473 nm excitation, and inductively-coupled plasma-optical emission spectrometry (ICP-OES; Varian, 720ES). Average particle diameter can be calculated from a specific surface area (SSA), which was measured by Brunauer–Emmett–Teller (BET) nitrogen adsorption (Micromeritics, ASAP 2420). Surface chemistry was identified using X-ray photoelectron spectroscopy (XPS). Light absorbance was measured using ultraviolet-visible spectroscopy (UV-vis, Varian, Cary 500) and a superconducting quantum interference device-vibrating sample magnetometer (SQUID-VSM, Quantum design, USA) was used for the magnetic properties.

The nanoparticle morphology and size were extracted from transmission electron microscope results (TEM, FEI Com., Titan 80-300ST) by operating it at an accelerating voltage of 300 kV. The microscope was set in various modes, such as bright-field TEM (BF-TEM), high resolution TEM (HRTEM), selected area electron diffraction (SAED), core-loss electron energy-loss spectroscopy (EELS), and energy-filtered TEM (EFTEM) modes to obtain specific information about the physical properties of Fe-doped TiO_2 nanoparticles. The entire TEM data were obtained and resolved by Digital-Micrograph Software Package (Gatan Inc., Version GMS1.85).

5. Conclusions

Flame spray pyrolysis was utilized to synthesize pure and Fe-doped TiO_2 nanoparticles with various iron concentrations in a single-step process. Ferrocene was mixed with TTIP and used as the precursor for iron-doped TiO_2 . XRD and Raman confirmed that the anatase phase was dominant in pure TiO_2 nanoparticles (>90% anatase), with an average particle diameter of about 12 nm (based on HRTEM). The addition of iron substantially changed the anatase phase to rutile with the anatase percentage decreasing from 86% to 21% when the Fe/Ti atomic ratio in the sample was changed from 1% to 10%, respectively. Morphology of the generated nanoparticles was studied using HRTEM, which revealed the crystallinity of the spherical particles and the uniformity of Fe doping distribution across the samples. XPS confirmed the formation of Fe^{3+} and Fe^{2+} within the Fe-doped TiO_2 samples. The ratio of $\text{Fe}^{3+}/\text{Fe}^{2+}$ varied from 0.5 at Fe/Ti ratio of 3% to 1.8 at a 10% ratio. The valence band edge for the Fe-doped TiO_2 was also lowered by $\sim 1 \text{ eV}$ when compared to the pure TiO_2 sample. Regarding magnetic properties, Fe doping of TiO_2 nanoparticles changed the material from nonmagnetic to paramagnetic. Doping TiO_2 particles with Fe remarkably increased light absorption and expanded it to the visible-light region due to their narrower band gap. The iron-doped samples showed much higher catalytic activity for dye degradation under visible-light radiation when compared to pure

TiO₂ nanoparticles. Non-toxic, cost-effective photo-catalysts are vital for industrial waste water treatment.

In summary, FSP is an attractive method for the production of Fe-doped TiO₂ with ferrocene as the source of iron. The resulting material has desirable magnetic and optical properties, which can be used in various photocatalytic and electronic applications.

Author Contributions: Conceptualization, M.A.I. and S.H.C.; Data curation, M.A.I., M.N.H., D.H.A. and V.S.; Formal analysis, M.A.I., M.N.H., D.H.A. and V.S.; Funding acquisition, S.H.C.; Investigation, M.A.I., D.H.A.; Methodology, M.A.I., M.N.H., D.H.A. and V.S.; Supervision, S.H.C.; Visualization, M.A.I.; Writing—original draft, M.A.I.; Writing—review & editing, M.A.I., M.N.H., D.H.A., V.S. and S.H.C. All authors have read and agreed to the published version of the manuscript.

Funding: This work was supported by King Abdullah University of Science and Technology (KAUST) under a CCF Grant.

Data Availability Statement: The data presented in this study are available on request from the corresponding author.

Acknowledgments: The authors are grateful to Nasir Memon for his fruitful discussions and comments during the experimental phase of this work.

Conflicts of Interest: The authors declare no conflict of interest.

References

- Schimmöeller, B.; Pratsinis, S.E.; Baiker, A. Flame aerosol synthesis of metal oxide catalysts with unprecedented structural and catalytic properties. *ChemCatChem* **2011**, *3*, 1234–1256. [[CrossRef](#)]
- Wegner, K.; Schimmöeller, B.; Thiebaut, B.; Fernandez, C.; Rao, T.N. Pilot plants for industrial nanoparticle production by flame spray pyrolysis. *KONA Powder Part J.* **2011**, *29*, 251–265. [[CrossRef](#)]
- Teoh, W.Y.; Amal, R.; Mädler, L. Flame spray pyrolysis: An enabling technology for nanoparticles design and fabrication. *Nanoscale* **2010**, *2*, 1324–1347. [[CrossRef](#)] [[PubMed](#)]
- Anjum, D.H.; Memon, N.K.; Chung, S.H. Investigating the growth mechanism and optical properties of carbon-coated titanium dioxide nanoparticles. *Mater. Lett.* **2013**, *108*, 134–138. [[CrossRef](#)]
- Ismail, M.A.; Memon, N.K.; Mansour, M.S.; Anjum, D.H.; Chung, S.H. Curved wall-jet burner for synthesizing titania and silica nanoparticles. *Proc. Combust. Inst.* **2015**, *35*, 2267–2274. [[CrossRef](#)]
- Memon, N.K.; Anjum, D.H.; Chung, S.H. Multiple-diffusion flame synthesis of pure anatase and carbon-coated titanium dioxide nanoparticles. *Combust. Flame* **2013**, *160*, 1848–1856. [[CrossRef](#)]
- Luu, C.L.; Nguyen, Q.T.; Ho, S.T. Synthesis and characterization of Fe-doped TiO₂ photocatalyst by the sol–gel method. *Adv. Nat. Sci. Nanosci.* **2010**, *1*, 015008. [[CrossRef](#)]
- Yu, J.; Xiang, Q.; Zhou, M. Preparation, characterization and visible-light-driven photocatalytic activity of Fe-doped titania nanorods and first-principles study for electronic structures. *Appl. Catal. B* **2009**, *90*, 595–602. [[CrossRef](#)]
- Chen, D.; Jiang, Z.; Geng, J.; Wang, Q.; Yang, D. Carbon and nitrogen co-doped TiO₂ with enhanced visible-light photocatalytic activity. *Ind. Eng. Chem. Res.* **2007**, *46*, 2741–2746. [[CrossRef](#)]
- Wang, Z.; Wang, W.; Tang, J.; Spinu, L.; Zhou, W. Extraordinary Hall effect and ferromagnetism in Fe-doped reduced rutile. *Appl. Phys. Lett.* **2003**, *83*, 518–520. [[CrossRef](#)]
- Hirano, M.; Joji, T.; Inagaki, M.; Iwata, H. Direct formation of iron (III)-doped titanium oxide (anatase) by thermal hydrolysis and its structural property. *J. Am. Ceram. Soc.* **2004**, *87*, 35–41. [[CrossRef](#)]
- Zhang, Y.; Ebbinghaus, S.G.; Weidenkaff, A.; Kurz, T.; Krug von Nidda, H.-A.; Klar, P.J.; Güngerich, M.; Reller, A. Controlled iron-doping of macrot textured nanocrystalline titania. *Chem. Mater.* **2003**, *15*, 4028–4033. [[CrossRef](#)]
- Wang, X.; Li, J.-G.; Kamiyama, H.; Katada, M.; Ohashi, N.; Moriyoshi, Y.; Ishigaki, T. Pyrogenic iron (III)-doped TiO₂ nanopowders synthesized in RF thermal plasma: Phase formation, defect structure, band gap, and magnetic properties. *J. Am. Chem. Soc.* **2005**, *127*, 10982–10990. [[CrossRef](#)]
- Deng, L.; Wang, S.; Liu, D.; Zhu, B.; Huang, W.; Wu, S.; Zhang, S. Synthesis, characterization of Fe-doped TiO₂ nanotubes with high photocatalytic activity. *Catal. Lett.* **2009**, *129*, 513–518. [[CrossRef](#)]
- Teoh, W.Y.; Amal, R.; Mädler, L.; Pratsinis, S.E. Flame sprayed visible light-active Fe-TiO₂ for photomineralisation of oxalic acid. *Catal. Today* **2007**, *120*, 203–213. [[CrossRef](#)]
- Hirasawa, T.; Sung, C.-J.; Yang, Z.; Joshi, A.; Wang, H. Effect of ferrocene addition on sooting limits in laminar premixed ethylene–oxygen–argon flames. *Combust. Flame* **2004**, *139*, 288–299. [[CrossRef](#)]
- Zhang, J.; Megaridis, C.M. Soot suppression by ferrocene in laminar ethylene/air nonpremixed flames. *Combust. Flame* **1996**, *105*, 528–540. [[CrossRef](#)]

18. Vander Wal, R.L.; Hall, L.J. Ferrocene as a precursor reagent for metal-catalyzed carbon nanotubes: Competing effects. *Combust. Flame* **2002**, *130*, 27–36. [[CrossRef](#)]
19. Kuwana, K.; Saito, K. Modeling ferrocene reactions and iron nanoparticle formation: Application to CVD synthesis of carbon nanotubes. *Proc. Combust. Inst.* **2007**, *31*, 1857–1864. [[CrossRef](#)]
20. Fotou, G.P.; Scott, S.J.; Pratsinis, S.E. The role of ferrocene in flame synthesis of silica. *Combust. Flame* **1995**, *101*, 529–538. [[CrossRef](#)]
21. Aguilar-Elguézabal, A.; Antúnez, W.; Alonso, G.; Delgado, F.P.; Espinosa, F.; Miki-Yoshida, M. Study of carbon nanotubes synthesis by spray pyrolysis and model of growth. *Diam. Relat. Mater.* **2006**, *15*, 1329–1335. [[CrossRef](#)]
22. Afre, R.A.; Soga, T.; Jimbo, T.; Kumar, M.; Ando, Y.; Sharon, M. Growth of vertically aligned carbon nanotubes on silicon and quartz substrate by spray pyrolysis of a natural precursor: Turpentine oil. *Chem. Phys. Lett.* **2005**, *414*, 6–10. [[CrossRef](#)]
23. Nandiyanto, A.B.D.; Kaihatsu, Y.; Iskandar, F.; Okuyama, K. Rapid synthesis of a BN/CNT composite particle via spray routes using ferrocene/ethanol as a catalyst/carbon source. *Mater. Lett.* **2009**, *63*, 1847–1850. [[CrossRef](#)]
24. Hafshejani, L.D.; Tangsir, S.; Koponen, H.; Riikonen, J.; Karhunen, T.; Tapper, U.; Lehto, V.-P.; Moazed, H.; Naseri, A.A.; Hooshmand, A. Synthesis and characterization of Al₂O₃ nanoparticles by flame spray pyrolysis (FSP)-role of Fe ions in the precursor. *Powder Technol.* **2016**, *298*, 42–49. [[CrossRef](#)]
25. Inamdar, S.N.; Haram, S.K. Synthesis and characterization of uncapped γ -Fe₂O₃ nanoparticles prepared by flame pyrolysis of ferrocene in ethanol. *J. Nanosci. Nanotechnol.* **2006**, *6*, 2155–2158. [[CrossRef](#)]
26. Chahar, M.; Pathak, D.K.; Thakur, O.P.; Vankar, V.D.; Kumar, R. Deposition of single phase polycrystalline α -Fe₂O₃ thin film on silicon and silica substrates by spray pyrolysis. *Silicon* **2020**, 1–6. [[CrossRef](#)]
27. Akurati, K.K.; Vital, A.; Klotz, U.E.; Bommer, B.; Graule, T.; Winterer, M. Synthesis of non-aggregated titania nanoparticles in atmospheric pressure diffusion flames. *Powder Technol.* **2006**, *165*, 73–82. [[CrossRef](#)]
28. Schulz, H.; Madler, L.; Strobel, R.; Jossen, R.; Pratsinis, S.E.; Johannessen, T. Independent control of metal cluster and ceramic particle characteristics during one-step synthesis of Pt/TiO₂. *J. Mater. Res.* **2005**, *20*, 2568–2577. [[CrossRef](#)]
29. Soria, J.; Conesa, J.; Augugliaro, V.; Palmisano, L.; Schiavello, M.; Sclafani, A. Dinitrogen photoreduction to ammonia over titanium dioxide powders doped with ferric ions. *J. Phys. Chem.* **1991**, *95*, 274–282. [[CrossRef](#)]
30. Li, W.; Ni, C.; Lin, H.; Huang, C.; Shah, S.I. Size dependence of thermal stability of TiO₂ nanoparticles. *J. Appl. Phys.* **2004**, *96*, 6663–6668. [[CrossRef](#)]
31. Sun, L.; Lin, J.X.; Wang, L.; Song, K.X. Preparation and characterization of Fe³⁺-doped TiO₂/diatomite composite. *Appl. Mech. Mat.* **2013**, *268–270*, 15–18. [[CrossRef](#)]
32. Chen, H.X.; Dobbins, R.A. Crystallogenesis of particles formed in hydrocarbon combustion. *Combust. Sci. Technol.* **2000**, *159*, 109–128. [[CrossRef](#)]
33. Mikaeili, F.; Topcu, S.; Jodhani, G.; Gouma, P.-I. Flame-sprayed pure and Ce-doped TiO₂ photocatalysts. *Catalysts* **2018**, *8*, 342. [[CrossRef](#)]
34. Anjum, D.H.; Memon, N.K.; Ismail, M.; Hedhili, M.N.; Sharif, U.; Chung, S.H. Transmission electron microscopy of carbon-coated and iron-doped titania nanoparticles. *Nanotechnology* **2016**, *27*, 365709. [[CrossRef](#)]
35. Biesinger, M.C.; Lau, L.W.; Gerson, A.R.; Smart, R.S.C. Resolving surface chemical states in XPS analysis of first row transition metals, oxides and hydroxides: Sc, Ti, V, Cu and Zn. *Appl. Surf. Sci.* **2010**, *257*, 887–898. [[CrossRef](#)]
36. Fujii, T.; De Groot, F.; Sawatzky, G.; Voogt, F.; Hibma, T.; Okada, K. In situ XPS analysis of various iron oxide films grown by NO₂-assisted molecular-beam epitaxy. *Phys. Rev. B* **1999**, *59*, 3195. [[CrossRef](#)]
37. Barreca, D.; Battiston, G.A.; Berto, D.; Gerbasi, R.; Tondello, E. Chemical vapor deposited Fe₂O₃ thin films analyzed by XPS. *Surf. Sci. Spectra* **2001**, *8*, 240–245. [[CrossRef](#)]
38. Aronniemi, M.; Sainio, J.; Lahtinen, J. Chemical state quantification of iron and chromium oxides using XPS: The effect of the background subtraction method. *Surf. Sci.* **2005**, *578*, 108–123. [[CrossRef](#)]
39. Bapna, K.; Phase, D.; Choudhary, R. Study of valence band structure of Fe doped anatase TiO₂ thin films. *J. Appl. Phys.* **2011**, *110*, 043910. [[CrossRef](#)]
40. Chen, B.; Haring, A.J.; Beach, J.A.; Li, M.; Doucette, G.S.; Morris, A.J.; Moore, R.B.; Priya, S. Visible light induced photocatalytic activity of Fe³⁺/Ti³⁺ co-doped TiO₂ nanostructures. *RSC Adv.* **2014**, *4*, 18033–18037. [[CrossRef](#)]
41. Balcells, L.; Frontera, C.; Sandiumenge, F.; Roig, A.; Martínez, B.; Kouam, J.; Monty, C. Absence of ferromagnetism in Fe-doped TiO₂ nanoparticles. *Appl. Phys. Lett.* **2006**, *89*, 122501. [[CrossRef](#)]
42. Janisch, R.; Gopal, P.; Spaldin, N.A. Transition metal-doped TiO₂ and ZnO-present status of the field. *J. Phys. Condens. Matter* **2005**, *17*, R657. [[CrossRef](#)]
43. Coey, J.M.D.; Stamenov, P.; Gunning, R.; Venkatesan, M.; Paul, K. Ferromagnetism in defect-ridden oxides and related materials. *New J. Phys.* **2010**, *12*, 053025. [[CrossRef](#)]
44. Suryanarayanan, R.; Naik, V.M.; Kharel, P.; Talagala, P.; Naik, R. Room temperature ferromagnetism in spin-coated anatase-and rutile-Ti_{0.95}Fe_{0.05}O₂ films. *J. Phys. Condens. Matter* **2005**, *17*, 755. [[CrossRef](#)]
45. Coey, J.; Wongsaprom, K.; Alaria, J.; Venkatesan, M. Charge-transfer ferromagnetism in oxide nanoparticles. *J. Phys. D Appl. Phys.* **2008**, *41*, 134012. [[CrossRef](#)]
46. Choi, W.; Termin, A.; Hoffmann, M.R. The role of metal ion dopants in quantum-sized TiO₂: Correlation between photoreactivity and charge carrier recombination dynamics. *J. Phys. Chem.* **1994**, *98*, 13669–13679. [[CrossRef](#)]

47. Zhu, J.; Zheng, W.; He, B.; Zhang, J.; Anpo, M. Characterization of Fe-TiO₂ photocatalysts synthesized by hydrothermal method and their photocatalytic reactivity for photodegradation of XRG dye diluted in water. *J. Mol. Catal. Chem.* **2004**, *216*, 35–43. [[CrossRef](#)]
48. Yang, X.; Cao, C.; Erickson, L.; Hohn, K.; Maghirang, R.; Klabunde, K. Photo-catalytic degradation of Rhodamine B on C-, S-, N-, and Fe-doped TiO₂ under visible-light irradiation. *Appl. Catal. B* **2009**, *91*, 657–662. [[CrossRef](#)]
49. Aarthi, T.; Madras, G. Photocatalytic degradation of rhodamine dyes with nano-TiO₂. *Ind. Eng. Chem. Res.* **2007**, *46*, 7–14. [[CrossRef](#)]
50. Fu, H.; Pan, C.; Yao, W.; Zhu, Y. Visible-light-induced degradation of rhodamine B by nanosized Bi₂WO₆. *J. Phys. Chem. B* **2005**, *109*, 22432–22439. [[CrossRef](#)] [[PubMed](#)]